JOURNAL OF THERMOPHYSICS AND HEAT TRANSFER
Vol. 23, No. 4, October–December 2009

Computational Modeling of a Segmented-Involute-Foil Regenerator for Stirling Engines

Mounir B. Ibrahim* and Daniel Danila†
Cleveland State University, Cleveland, Ohio 44115
Terrence W. Simon‡
University of Minnesota, Minneapolis, Minnesota 55455
David Gedeon§
Gedeon Associates, Athens, Ohio, 45701
and
Roy Tew¶
NASA John H. Glenn Research Center at Lewis Field, Cleveland, Ohio 44135

DOI: 10.2514/1.40330

A microfabricated, segmented-involute-foil regenerator was numerically investigated using the Fluent commercial software under both steady- and oscillatory-flow conditions and using two- and three-dimensional numerical simulations. Steady-state simulations were performed for $Re = 50$–2000. The oscillatory-flow conditions were performed for $Re_{\max} = 50$ and $Re_{\omega} = 0.229$, with the hot end at 310 K and the cold end at 293 K. For the steady-state three-dimensional simulation, both the local friction factor and the local mean Nusselt numbers started to depart from the two-dimensional simulation values upon entering the second layer. At the entrance of every layer, the forced reorientation of the flow results in small rises of both the friction factor and the mean Nusselt number, with subsequent decrease as the flow settles into the new layer. As for the oscillatory-flow simulations, the two-dimensional model was used to study the effects of changing 1) the oscillation amplitude and frequency, 2) the thermal contact resistance between layers, and 3) the solid material. The effects of these parameters on the total regenerator heat loss (convection and conduction) were documented and are expected to be a useful tool for further development of Stirling engine regenerators.

Nomenclature

D_h, d_h	=	matrix hydraulic diameter, m
f_D	=	Darcy friction factor $= (\Delta p D_h)/[\rho(u_m^2/2)\Delta x]$
f_F	=	fanning friction factor $= f_D/4$
Nu	=	Nusselt number $= hD_h/k$
Nu_m	=	mean Nusselt number $= h_m D_h/k$
Nu_x	=	local Nusselt number $= h_x D_h/k$
Pe	=	Peclet number $= RePr$
Pr	=	Prandtl number
Re	=	Reynolds number
$Re_{\max}$	=	maximum Reynolds number $= u_{m,\max} D_h/\nu$
Re_{ω}, Va	=	Valensi number $= \omega D_h^2/4\nu$
T	=	temperature, °C
T_c	=	cold end temperature, °C
T_h	=	hot end temperature, °C
t	=	time, s
$u_{\max}$	=	maximum bulk mean velocity in regenerator, m/s
x	=	axial distance, m
x^+	=	dimensionless length used for friction-factor plots $= x/D_h Re$
x^*	=	dimensionless length used for Nusselt number plots $= x/D_h Re\, Pr$
β	=	porosity
Δp	=	pressure drop, Pa
θ	=	crank angle, deg
μ	=	dynamic viscosity, kg/m · s
ν	=	kinematic viscosity, m^2/s
ρ	=	density, kg/m^3
ω	=	angular frequency, rad/s

Received 8 August 2008; revision received 4 April 2009; accepted for publication 16 April 2009.

*Professor, Mechanical Engineering Department, 1960 East 24th Street, Room 261, Stillwell Hall. Associate Fellow AIAA.
†Graduate Student, Mechanical Engineering Department, 1960 East 24th Street, Room 261, Stillwell Hall.
‡Professor, Mechanical Engineering Department, 111 Church Street Southeast. Member AIAA.
§President, 16922 South Canaan Road.
¶Research Engineer, Thermal Energy Conversion Branch, 21000 Brookpark Road, Mail Stop 301-2. Member AIAA.

I. Introduction

THE Stirling engine regenerator has been called "the crucial component" (Organ [1]) in the Stirling cycle engine. The regenerator, which obtains heat from the hot working fluid and releases heat to the cold working fluid, recycles the energy internally, allowing the Stirling cycle to achieve high efficiency. The location of the regenerator within a Stirling convertor is shown in Fig. 1.

Currently, regenerators are usually made of woven screens or random fibers. Woven-screen regenerators have relatively high flow friction. They also require long assembly times which tend to increase their cost. Random-fiber regenerators also have high flow friction but are easy to fabricate and are therefore inexpensive. Figure 2 shows a typical random-fiber annular regenerator, and Fig. 3 shows a close-up of the fibers. Because of the method of fabrication, the fibers are random primarily in a plane perpendicular to the main flowpath. Thus, both woven screens and random fibers experience flow primarily across the wires (cylinders in crossflow). Cylinders in crossflow tend to cause flow separation resulting in high flow friction and considerable thermal dispersion, a thermal loss mechanism that causes an increase in apparent axial thermal conduction. For space engines, there must be assurance that no fibers of this matrix will eventually work loose and damage vital convertor parts during the mission. It is also important that local variations in porosity inherent to random-fiber regenerators not result in local mismatches in flow channels, which would contribute to axial thermal transport. Wire

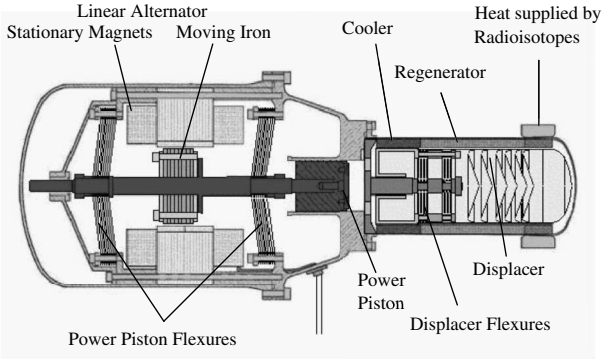

Fig. 1 Schematic of Stirling convertor showing the location of the regenerator.

screens have some randomness associated with their stacking and thus may have locally nonuniform flow. The efforts thus far have shown that attractive features for effecting high fluid-to-matrix heat transfer with low-pressure drop are a matrix in which 1) the heat-transfer surface is smooth, 2) the flow acceleration rates are controlled, 3) flow separation is minimized, and 4) passages are provided to allow radial mass flow for a more uniform distribution when the inlet flow or the in-channel characteristics are not radially uniform. It is thought that properly designed microfabricated regular geometries could not only reduce pressure drop, maintain high heat transfer, and allow some flow redistribution when needed, but could also show improved regenerator durability for long missions.

Recently, Cleveland State University (CSU), the University of Minnesota (UMN), Gedeon Associates, Infinia Corp., Sunpower, Inc., and International Mezzo Technologies (Mezzo) have been collaborating via a Radioisotope-Power-Conversion Technology, NASA Research Award contract. The project brought together experts in Stirling cycle machine design, microfabrication processing, oscillatory-fluid-flow experimentation, and computational fluid dynamics (CFD) to design and fabricate an advanced regenerator matrix for use in Stirling cycle space–power conversion technology. The main objectives were to significantly reduce the pressure drop of the regenerator while maintaining its thermal efficiency (thus improving the power and efficiency of the Stirling convertor) and to improve the structural reliability and manufacturability of the regenerator. In addition to the benefit to Stirling convertor space–power technology, such regenerator development will also benefit Stirling cycle coolers and NASA's many cryocooler-enabled missions.

CFD analysis for different geometries was employed to model the fluid flow and heat transfer under both steady and oscillatory-flow conditions. The effects of surface roughness were included [2]. Several geometries, including lenticular [3], parallel plates (equally/nonequally spaced), staggered parallel plates (equally/nonequally spaced), and 3-D involute foils were studied via CFD. The modeling was applied to both the microscale involute-foil regenerator and to the large-scale mock-up (LSMU) model of it.

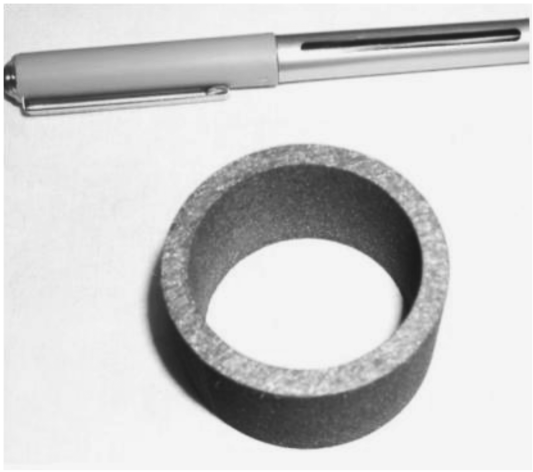

Fig. 2 Random-fiber regenerator.

A NASA contract report (Ibrahim et al. [4]) documents the details of this project, including 1) fabrication and testing of a microscale involute-foil regenerator, 2) a LSMU, 30 times the actual scale, of the experimental model and the data obtained from it, and 3) analyses of the newly designed regenerator via 1-D, 2-D, and 3-D computational techniques. Several publications (some already published [5,6]) are underway to focus on the different aspects of the project. In this paper, we will focus on the CFD efforts to model the actual-size regenerator and the LSMU. These computational tools enabled evaluating 1) the figure of merit and 2) the effect of varying different parameters such as solid material used, thermal contact resistance (TCR) between the regenerator layers, etc., for the new design.

II. Description of the Actual-Size Regenerator and Its Large-Scale Mock-Up

The actual-size regenerator (see Figs. 4a and 4b) consists of a stack (42 layers) of involute-foil disks (or annular portions of disks) that have been microfabricated by the LiGA/EDM processes, where LiGA is Lithographie, Galvanoformung, and Abformung (the German words for lithography, electroplating, and molding; x-ray lithography is used here) and EDM is electric discharge machining. This regenerator has a low resistance to flow because it has a reduced number of separation regions compared to wire screen and random fiber. However, it still has high-heat-transfer effectiveness approaching that of the other structures. The resulting figure of merit (proportional to the ratio of heat transfer to pressure drop) has proven superior to the currently used random-fiber and wire-screen regenerator structures. It has known small features which are secured to the assembly so that it is not as susceptible to releasing small fragments of regenerator matrix material (as random fiber and wire screen, both of which have random features).

The LSMU testing was based on dimensions 30 times the actual size and test conditions dynamically similar to those expected in an engine (see Fig. 5). The LSMU was fabricated and tested at UMN.

Figure 6 shows a progressively exploded flow-direction view of one of the involute-foil regenerator disks. On the second zoom, the channels can be seen more clearly. The disk portrayed in Fig. 6 has six ribs. There is a second type of disk that has seven ribs. This enables the staggering of the ribs in the stack to reduce axial conduction and improve axial channeling of the flow.

Figure 7 shows a 3-D view of only one channel of one layer with dimension labels. It can be seen in this figure that the walls of the channel are curved with an involute-foil profile. Table 1 shows involute-foil channel dimensions and the segment or layer length (thickness, in the table). Note that the channel width W given in Table 1 is a nominal value; as can be seen in the middle view of Fig. 6, W varies somewhat from the inner to the outer ring of each layer of the actual-size involute-foil segments (this variation of W is also true for the large-scale segmented involute foils of the LSMU, as can be seen in Fig. 5).

This design has several potential advantages compared to existing designs (such as random-fiber and wire-screen matrices) as demonstrated by Sage and finite element analyses done earlier [4] and the actual microfabricated hardware and test results; these advantages are summarized as follows: 1) improved ratio of heat transfer to pressure drop, that is, high figure of merit, 2) low axial conduction due to minimal contact area between disks, 3) better reproducibility and control over geometric parameters, and 4) high structural integrity and durability.

It was a challenge to analyze this geometry for fluid flow and heat transfer via CFD so as to facilitate the comparison between this geometry and other regenerator geometries. The first difficulty is the complex 3-D geometry, as depicted in Fig. 4b. The second is the oscillatory nature of the flow as it occurs in the Stirling engine.

In this paper, a description will be given for the modeling setup used to analyze the problem. This includes the grid generation for the

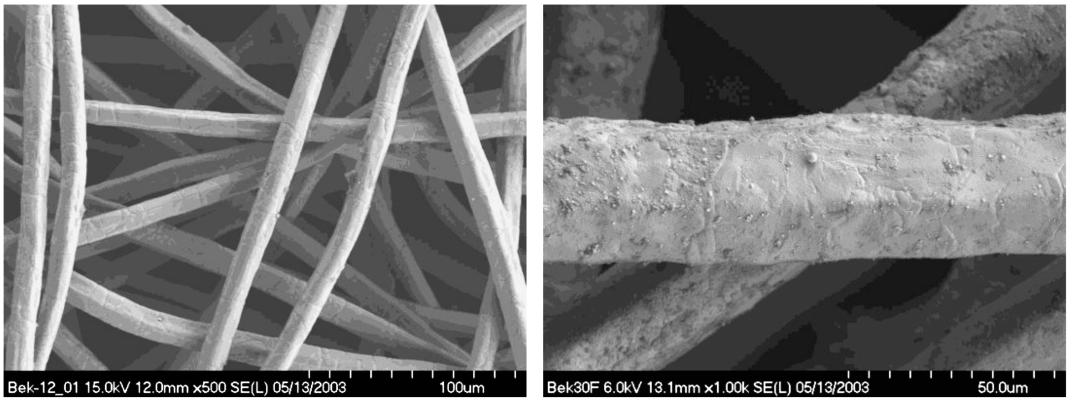

Fig. 3 Electron micrography of a random-fiber regenerator matrix. Courtesy of NASA John H. Glenn Research Center at Lewis Field.

computational domain and the matrix under investigation. Results of the numerical investigation for the different parameters of the proposed problem will be presented, followed by the conclusions.

III. Computational Fluid Dynamics Computational Domain

It was decided early on that it would not be feasible from a microscopic computational point of view to model the whole regenerator. Therefore, it was necessary to look for simplifications, which usually come in the form of symmetries and boundary-condition approximations. Accordingly, we took several progressive simplifying steps in analyzing the involute-foil matrix via CFD. Next is a brief description of each of the CFD models used, from more complex to simpler models. Fluent [7] commercial code was used in this investigation.

A. Model 1, Three-Dimensional Involute Channels

Employing the radial and angular periodicity of the geometry, we were able to build a model based on one sector (with 8.87 deg) and by applying periodic boundary conditions (B.C.) as shown in Fig. 8.

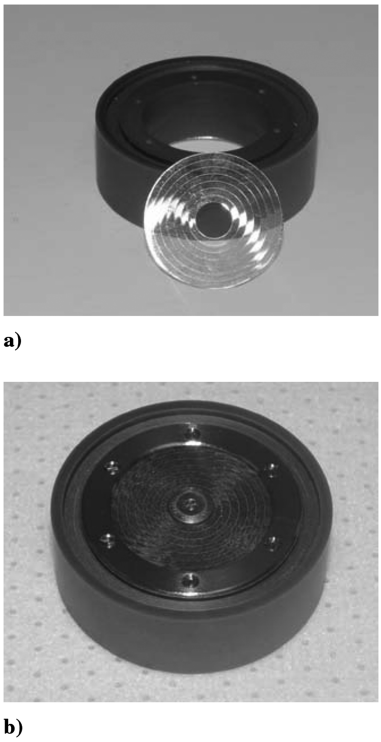

a)

b)

Fig. 4 Actual-size involute-foil regenerator: a) disk leaning against outer housing, and b) assembled (stack of 42 disks).

Figure 9 shows an enlarged area from the middle of the sector of Fig. 8. In Fig. 9, one can see the channel walls, the angle formed between channel walls (81 deg in this middle ring) in two successive layers, and how the involute-foil profile of the wall deviates from a flat wall (by about 2 deg). This figure suggests possible further simplification of the geometry by approximating the involute-foil profile with a straight line and the angle between successive layer walls to a right angle (this will be discussed later).

The regenerator is a stack of layers that can be represented by two types of alternating layers; those two layers represent a repeating unit. One can use the flow output of one repeating unit as the input to the next one, and so on. Figure 10 shows an isometric view of three successive layers (or, more precisely, four boundaries of these three layers). Because the frontal area occupied by the circular ribs is very small in comparison to the rest of the frontal area, a simplification was made to line up the ribs from disk to disk. In the real geometry, the ribs are staggered from disk to disk. The orientation (crossing angle) of the channel walls was not significantly altered by the alignment of the ribs. As shown in Fig. 10, the ribs of two successive layers are aligned, but the channel walls are still approximately perpendicular from layer to layer. Aligning the ribs enables a bounded domain in the radial direction for both layers which forms a repeating unit.

As mentioned earlier, the minimum thickness of the repeating unit has to be the thickness of two layers. However, the interface between two layers is a geometric discontinuity. The exit (velocities and temperatures profiles) of one repeating unit would be used as a boundary inlet to the next one. It is better to have no geometric discontinuities at boundary inlets and outlets. Therefore, the selected repeating unit consisted of half the thickness of one layer, followed by a full-thickness layer, and ending in another half-thickness of the next layer. So, a half-layer thickness was used at the entry and exit. Figure 11 shows this arrangement.

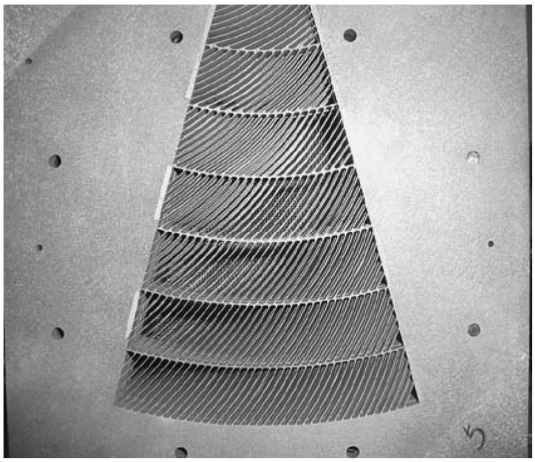

Fig. 5 Picture of five aligned LSMU plates.

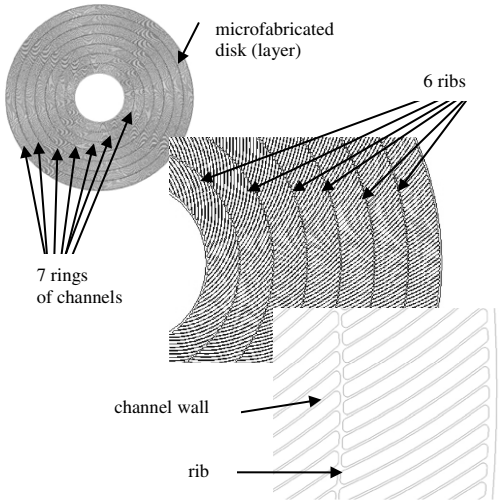

Fig. 6 Exploded view of the microfabricated disk.

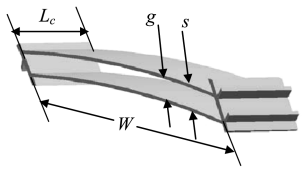

Fig. 7 Segmented-involute-foil channel of one layer.

B. Model 2, Three-Dimensional Straight Channels

Flow direction periodicity works only for steady-state modeling. The transient simulation for the case studied requires oscillatory (alternating-direction, zero-mean) flow, requiring a stack of several layers to be included in the domain. A minimum of six layers was determined to be adequate to capture the oscillatory-flow phenomena. However, even if radial and angular periodicities are employed, the grid size would still be too large for the available computation capability. Further simplifications, as indicated in Fig. 12, must be used. If the foil-crossing angle from one layer to the next is approximated to 90 deg (instead of 81), the involute-foil profile is approximated as straight, and the round ends of the channels are neglected, then one can build a manageable grid. This is expected to capture most of the 3-D oscillatory-flow phenomena of the microfabricated design. Figure 12 shows such a computational domain.

Table 2 shows dimensions of the computational domain shown in Fig. 12. To maintain the same hydraulic diameter as the actual involute-foil geometry, the gap was adjusted to 81 μm from 84 (see Table 1). To maintain the same spacing, the wall thickness was adjusted to 19 μm from 16. Another adjustment was made to the layer thickness which was decreased from 265 to 250 μm. This was done to better match the actual disks that were fabricated for experimental testing, because the original design called for 265 μm thick disks, but the manufacturer (Mezzo) fabricated 250 μm thick disks. The resulting porosity, as shown in Table 2, was 0.81 instead of the actual regenerator's 0.84.

Table 1 Involute-foil channel dimensions

Dimension	Unit	Value
Gap, g	micron, 10^{-6} m	86
Gap + wall, s	micron	100
Wall thickness, s-g	micron	14
Channel width, W	micron	1000
Disk (layer, segment) thickness, L_c	micron	265
Porosity	——	0.838
Hydraulic diameter, D_h	micron	162

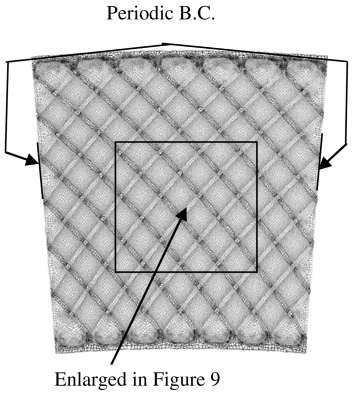

Fig. 8 Periodic sector from Fig. 6, showing two layers with computational grids.

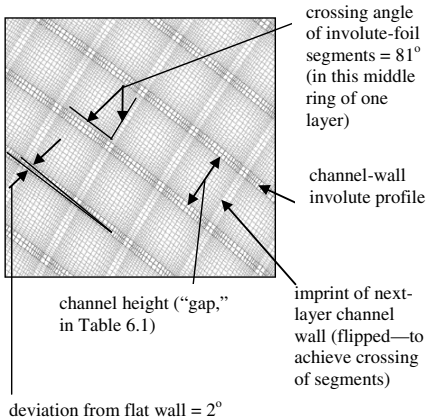

Fig. 9 Enlarged area in the middle of the periodic sector.

C. Model 3, Two-Dimensional Computational Domain

Further simplifications were also made, for part of the CFD study, by using a 2-D computational domain. For the cases studied, the 2-D domain consisted of a single parallel-plate channel and solid walls with six successive sections. There was no variation in flow geometry upon exiting one section and entering the next. However, by changing the solid-interface settings, one could set various values for the TCR between wall sections. This was expected to capture the interruption in the wall thermal conduction that is obtained by alternating the orientation of the channel walls (from one layer to the next) in the 3-D domain. Figure 13 shows such a 2-D computational domain. This 2-D domain allowed for quick parametric studies and finding trends that could be later confirmed in 3-D with fewer runs.

D. Code Validation for All Models

As presented in the preceding subsections, three different models were identified for dealing with the geometry under investigation. Model 1 is 3-D for involute-foil layers, model 2 is 3-D straight-channel layers, and model 3 is 2-D straight channels. They represent different levels of compromise between the actual problem and the resources required to model the problem. Table 3 lists the three different models, the cell count employed in each, and the studies conducted using each one.

In model 1, over 5 million cells were used for steady flow runs and $Re = 50, 94, 183, 449, 1005$, and 2213. The solid material applied is stainless steel (SS) and zero TCR was applied between layers. There are no data, to the best of our knowledge, available in the open literature for the variation of f and/or Nu along the flow direction. The only f and Nu data available are for the whole stack [UMN data, Eqs. (3) and (4), and Kays and London [8]]. Therefore, those data were used to validate the model (as shown later). Another way of validating this model is to compare its results with 2-D data (model 3) only in the first layer (shown later).

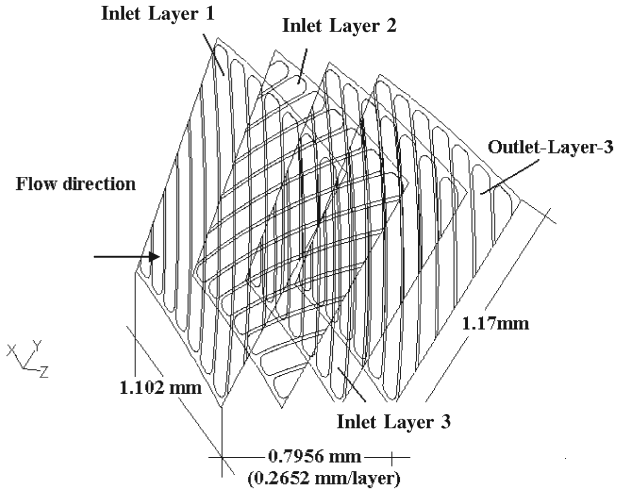

Fig. 10 Isometric view of four of the boundaries of three successive layers.

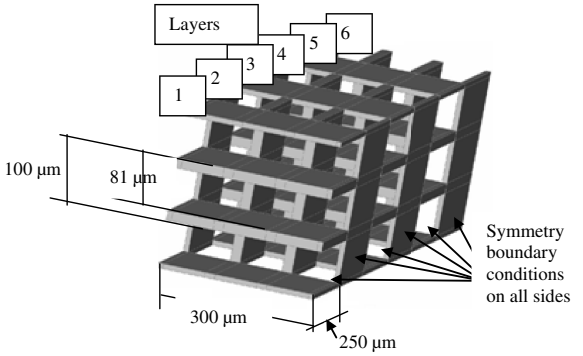

Fig. 12 Model 2, 3-D straight-channel layers computational domain, for six layers.

In model 2, over 3.5 million cells were used for steady ($Re = 50$) and oscillatory flow ($Re_{\max} = 50$ and $Re_{\omega} = 0.229$). The solid materials applied are SS and nickel. Zero and infinite TCRs were applied between layers. Again, for those 3-D cases, there are no data (to the best of our knowledge) available in the open literature for the variation of f and/or Nu along the flow direction. The only f and Nu data available are for the whole stack. Therefore, for oscillatory flow [Eqs. (4) and (5)], were used (as shown later). The model matches Eq. (4) very well. As for steady-state cases, we used Eqs. (1) and (2) (as shown later). Because Eqs. (1) and (2) are obtained for 2-D geometries, we only expect the validation to take place for the first layer only, as shown later.

Model 3 uses 15,600 cells for steady ($Re = 50$, 150, and 1000) and oscillatory flow ($Re_{\max} = 50$ and 150, and $Re_{\omega} = 0.229$ and 0.687). The solid materials applied are SS and nickel. Zero and infinite TCRs were applied between layers. For the steady-state cases, Eqs. (1) and (2) were used for the code validation (as shown later). As for the oscillatory flow, Eqs. (4) and (5) were used (as shown later).

The way we built the computation grids (grid independence) for the three models is from the 2-D up to the 3-D. Therefore, a grid-independence study was conducted (see Sec. VI) for the 2-D model (model 3) with 15,600 cells. Then, the 3-D models were extended to over 3.6 million cells for model 2 and over 5.4 million cells for model 1.

E. Boundary Conditions

The problem under investigation involves 3-D (models 1 and 2) and 2-D (model 3) computational models under steady and oscillatory-flow conditions. The 3-D models represent islands within the larger regenerator stack-up; the other boundaries (boundaries that are not inlets or outlets) are either symmetric or periodic in the case of the 8.87 deg slice, see Secs. IV.A and IV.B for more details. The TCRs between the solid layers (in models 2 and 3) were chosen as zero or infinity. The zero value is obtained by identifying these surfaces as interior in the Fluent code, whereas the infinity value was obtained by choosing an adiabatic boundary at those locations.

1. Steady-State Runs

For steady-state runs, the solid temperature was kept constant at 673 K while the fluid entered the channel at 660 K. Uniform inlet velocity was selected at the west boundary, whereas outlet pressure was chosen at the east boundary.

2. Oscillatory-Flow Runs

The running conditions for the base case examined in the oscillatory-flow study are shown in Table 4.

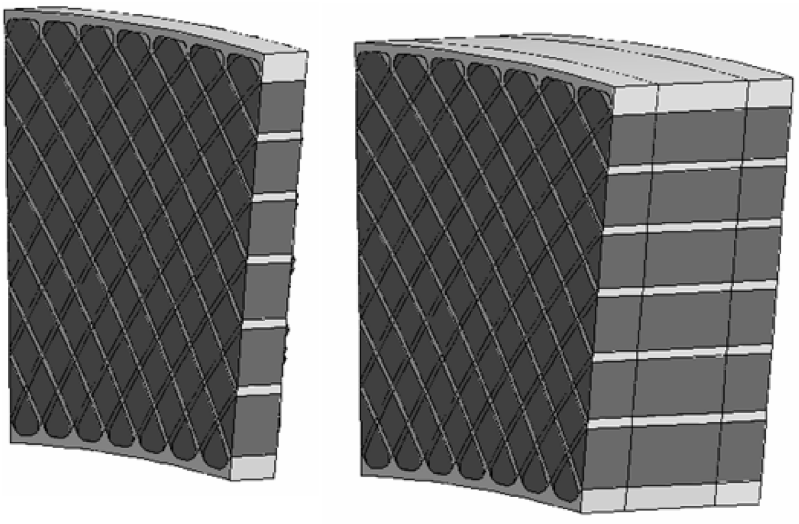

Fig. 11 Model 1, 3-D involute-foil layers computational domain, entry unit and repeating unit. The half-full half-computational domain unit can be repeated periodically until the required stack height is achieved.

Table 2 Three-dimensional straight-channel computational domain dimensions

Dimension	Unit	Value
Gap, g	micron, 10^{-6} m	81
Gap + wall, s	micron	100
Wall thickness, s-g	micron	19
Channel width, W	micron	300, symmetry
Disk (layer) thickness, L_c	micron	250
Porosity	——	0.81
Hydraulic diameter, D_h, $2g$	micron	162

IV. Friction Factor and Nusselt Number Correlations

The following correlations were used in this CFD study.

A. Steady State

1. Parallel Plate Friction Factor and Heat-Transfer Correlations

To compare the steady flow CFD results to the literature, the following correlations were selected from Shah and London [11]. The Fanning friction-factor correlation of Eq. (1) is attributed to Shah [9] and applies to laminar, hydrodynamically developing flow, the flow regime for the case studied:

$$f_F = \frac{1}{Re}\left(\frac{3.44}{(x^+)^{1/2}} + \frac{24 + (0.674/4x^+) - [3.44/(x^+)^{1/2})]}{1 + 0.000029(x^+)^{-2}}\right) \quad (1)$$

For steady heat transfer, the correlation of Eq. (2) was selected from Shah and London [11] and is attributed to Stephan [10]. This correlation applies to laminar, simultaneously (thermally and hydrodynamically) developing flow, which is the flow and thermal regime for the case studied. This correlation is valid for a constant wall temperature and Prandtl numbers between 0.1 and 1000:

$$Nu_m = 7.55 + \frac{0.024(x^*)^{-1.14}}{1 + 0.0358(x^*)^{-0.64}Pr^{0.17}} \quad (2)$$

2. Large-Scale Mock-Up Darcy Friction Factor

A study of the momentum equation noted that, for engine-representative Valensi and Reynolds numbers, the transient term is unimportant and pressure drop measurements can be taken as steady, unidirectional flow. Such measurements led to the following friction-factor correlation, Eq. (3), for the LSMU (Ibrahim et al. [4]):

$$f = \frac{153}{Re} + 0.127Re^{0.01} \quad (3)$$

B. Oscillatory Flow: Actual Scale

As for the oscillatory-flow cases, the following correlations, of Eqs. (4) and (5), for involute-foil friction factor and heat transfer are attributed to Gedeon (Ibrahim et al. [4]). These correlations were obtained from involute-foil experimental data. The experiments were done at Sunpower, Inc., on a NASA/Sunpower oscillating-flow test rig equipped with a microfabricated involute-foil regenerator. This regenerator had 42 disks in its stack (see Fig. 4). The material used for the disks was nickel:

$$f_D = \frac{117.3}{Re} + 0.38Re^{-0.053} \quad (4)$$

The range of key dimensionless groups for these tests are given in Table 5.

Heat transfer under oscillatory-flow conditions is given by

$$Nu_m = 1 + 1.97Pe^{0.374} \quad (5)$$

The range of key dimensionless groups for these tests is given in Table 6.

V. Computational Fluid Dynamics Grid-Independence Test and Code Validation

Three computational domains were identified as good candidates for modeling the problem at hand. One was a 2-D domain (model 3) and the other two were 3-D domains (models 1 and 2). The actual geometry (see Fig. 7) and range of Re (see Tables 5 and 6) indicate that a laminar, thermally, and hydrodynamically developing flow will adequately represent this case under investigation. As for the data available for code validation, the following were identified: 1) steady flow, 2-D geometry and local f [Eq. (1), Shah] and Nu [Eq. (2)] as functions of the axial flow location; 2) steady flow, 3-D geometry (LSMU) and mean values for f [Eq. (3)], and 3) oscillatory flow, 3-D geometry (actual scale) and mean values for f [Eq. (4)], and mean values for Nu [Eq. (5)]. Therefore, a strategy was developed to obtain a grid-independence test for the 2-D geometry (model 3). This geometry was used in the 3-D models (models 1 and 2). Thus, the availability of local f and Nu for 2-D geometry will ensure a good grid selection for the CFD experiments. Then, the 3-D geometry (as an extension for that grid) can be validated using mean f and Nu for steady and oscillatory-flow conditions.

The 2-D computational domains (model 3) with four different grid sizes were chosen. The number of grids (in the x direction X in the y direction, per layer) are as follows: 20×10, 30×20, 50×20, and 100×40. These are summarized in Table 7. Figure 14 shows the grid for the 20×10 grid only.

The aforementioned four grid sizes were tested and the results were plotted for friction factor as a function of dimensionless length x^+ for $Re = 150$ (see Fig. 15). Similarly, the results were plotted for mean Nusselt number Nu_m as a function of a different dimensionless length x^*, and also for $Re = 150$ (see Fig. 16). The results are poor for the smallest grid (20×10), although little gain in accuracy is achieved by moving from a grid size of 50×20 to 100×40. The 50×20 grid size was eventually selected as the best compromise between accuracy and computing resources, to be used following the completion of the grid-independence study. For more details, see Danila [12].

VI. Results of Two- and Three-Dimensional Modeling

The CFD results will be presented starting with 2-D, model 3, where extensive computations were conducted, followed by 3-D straight channel, model 2, and finally 3-D involute channel, model 1.

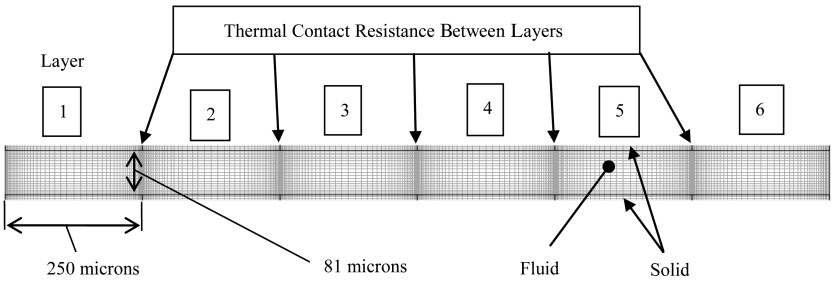

Fig. 13 Model 3, 2-D computational domain.

Table 3 Total cell count, conditions, *Re* number range for the different models examined

Model	Total cell count	Conditions examined	*Re* number range examined		Data (from literature) against which the model was validated
			Steady flow	Oscillatory flow	
Model 1, 3-D	5.40864×10^6	1) Solid material: SS	$Re = 50$, 94, 183, 449,	N/A	Eqs. (3) and (4), and Kays
		2) TCR between layers: 0	1005, and 2213		and London [8] (see Fig. 30).
Model 2, 3-D	3.6504×10^6	1) Solid material: SS and nickel	$Re = 50$	$Re_{\max} = 50$	**For steady state:**
		2) TCR between layers: 0 and ∞		$Re_\omega = 0.229$	Eqs. (1) and (2), see Figs. 22 and 23. Models 2 and 3 match very well in the first layer.
					For oscillatory flow:
					Eqs. (4) and (5), see Figs. 24 and 25. Model 2 matches Eq. (4) very well.
Model 3, 2-D	1.56×10^4	1) Solid material: SS and nickel	$Re = 50$, 150, and 1000	$Re_{\max} = 50$ and 150	**For steady state:**
		2) TCR between layers: 0 and ∞		$Re_\omega = 0.229$ and 0.687	Eqs. (1) and (2), see Figs. 22, 23, 27, and 28.
					For oscillatory flow:
					Eqs. (4) and (5), see Figs. 18, 19, 24, and 25.

Table 4 Base case for oscillatory-flow conditions

Valensi number, Re_ω	0.22885
Maximum Reynolds number, $Re_{\max}$	49.78
Frequency, Hz	27.98
Hydraulic diameter, m	0.000162
Max mass flux, $kg/m^2 \cdot s$	6.17215
Cold end solid B.C.	Adiabatic
Hot end solid B.C.	Adiabatic
Inlet fluid temperature, cold end, °K	293.1
Inlet fluid temperature, hot end, °K	310.2
Mean pressure, Pa	2.5×10^6
Mean, max velocity, m/s	1.5488

Table 5 Dimensionless parameter ranges for the pressure drop tests

Peak *Re* range	3.4–1190
Va range	0.11–3.8
δ/L range	0.13–1.3

Table 6 Dimensionless parameter ranges for heat transfer tests

Peak *Re* range	2.6–930
Va range	0.064–2.4
δ/L range	0.17–1.8

A. Results of Model 3, Two-Dimensional Computational Fluid Dynamics Simulations of Involute-Foil Layers

Steady state was examined first at $Re = 50$ to compare with available correlations. The comparison was good, especially at distances further away from the entrance. Then, oscillatory-flow cases were conducted to examine the effects (on friction factor and Nusselt number) of changing 1) the TCR between the six layers, 2) the oscillation amplitude, 3) the oscillation frequency, and 4) the type of solid material.

1. Base-Case Two-Dimensional Oscillatory Flow

For the oscillatory-flow simulations, the base-case forcing function, at 27.98 Hz, is

$$\text{mass flux} = 6.17215 \times \cos(2 \times \pi \times 27.98 \times t + 1.56556) \quad \text{kg/m}^2 \cdot \text{s} \tag{6}$$

This function is applied at the west (left) fluid boundary. Figure 17 shows the variation of the mass flux with the crank angle. All the following 2-D oscillatory-flow cases were run until cycle-to-cycle convergence was obtained and only after that were the data extracted.

For characterizing the oscillatory flow, the friction factor is compared with the experimental correlation [Eq. (4)] for the involute foil. The friction factor plotted versus the crank angle is shown in Fig. 18. The values obtained by the present simulation fall below the correlation. This was expected because the correlation was obtained from experimental results on an actual involute-foil regenerator, whereas the present 2-D simulation represents an idealized case, with flow through a foil channel that does not flow around foils in adjacent layers (i.e., there are no obstacles in the flowpath).

To characterize the heat transfer that takes place during an oscillatory-flow run, the mean Nusselt number is plotted with respect to the crank angle in Fig. 19. For comparison, the experimental mean Nusselt correlation [Eq. (5)] is used. However, this correlation represents a mean over the length of a stack of 42 layers tested in the oscillatory-flow rig at Sunpower, Inc. The present work focuses only on the region from the middle of layer 3 to the middle of layer 4. So the length over which the Nusselt number is averaged in the present work is equal to the thickness of one layer only. That is done to stay away from the ends where entrance effects can distort the results. On the other hand, calculating a mean Nusselt number over the length of

Table 7 Summary of grids tested in grid-independence study

Grids/axial segment	No. of cells between plates	Vertical grid-spacing ratio	No. of cells along axial segment (layer)	Horizontal or axial (segment) spacing ratio
20 × 10	10	1.15	20	1, uniform
30 × 20	20	1.15	30	1, uniform
50 × 20	20	1.1	50	1.1
100 × 40	40	1.1	100	1.05

six layers would not have been representative of the actual geometry. Furthermore, experimental testing done at the UMN looked at the mean Nusselt number calculated between two layers similar to what has been done in the present work. The shape of the mean Nusselt number Nu_m plot versus the crank angle is different from the Gedeon correlation, and this difference arises from how the Nusselt number is averaged. The experiments done at the UMN show a Nusselt number curve similar to the present work. However, the comparison with the Gedeon correlation is useful for the maximum Reynolds number regions that are located around 90 and 270 deg crank angle, where flow rates are maximum in the two directions. At these locations, the 2-D analysis lies slightly below the correlation.

By integrating the fluid enthalpy crossing a plane section in the middle of layer 3 over the whole cycle, one can calculate the net enthalpy loss over the cycle. If one integrates the solid-conduction heat transfer at the middle of layer 3 over the whole cycle, a net-conduction loss over the cycle can be obtained. Because both losses are crossing the plane at the middle of layer 3, they can be added together to obtain a total axial heat loss over the cycle. For the base-oscillatory-flow case, the 2-D CFD axial heat loss results are as follows: enthalpy loss 1.722 W, conduction loss 1.174 W, and total loss 2.896 W (these values will be used for a later comparison).

2. *Effect of Changing the Thermal Contact Resistance*

To study the effect of TCR between the layers, a change was made from the zero TCR of the base case to an infinite TCR at the interfaces between the layers (or from perfect thermal contact to perfect thermal insulation, between solid layers). The effect of TCR is important because, in reality, the contact between the layers is not perfect. This added contact resistance impedes the solid conduction from layer to layer. This contact resistance between the layers causes discontinuities in the solid wall temperature profile between the hot and cold sides of the interface. The changed wall temperature profile should affect the heat transfer between the wall and the fluid, which, in turn, should change the plot of the Nusselt number. However, the friction factor is not affected (as expected). Figure 20 shows a comparison of the Nusselt number behavior between the base case, zero TCR, and the infinite TCR.

The infinite TCR (adiabatic contact) has caused the Nusselt number to rise, especially in the regions of low Reynolds numbers close to where the flow reverses (near 180 and 360 deg crank angle). This was expected. When no TCR is present, the solid wall temperature on each side of the contact between the solid layers is the same. When the infinite TCR is introduced, a temperature difference takes place in the solid wall between the two sides of the contact area. The fluid flowing in the channel past the contact between the two solid layers shows the discontinuity in the wall temperature profile. The increased ΔT between the wall and the fluid causes an increase in the heat transfer and that is reflected in the higher Nusselt number. At lower Reynolds numbers, the fluid has more time to absorb the heat and the effect of the infinite TCR is more pronounced. However, when the flow stops, as it does when it switches direction, the temperature between the fluid and the solid equalizes and ΔT becomes very small, tending to zero. That introduces a discontinuity in the calculation of the Nusselt number, and Fig. 20 shows that discontinuity at 180 and 360 deg of crank angle. The other change that has happened is related to the difference between the cooling and the heating parts of the cycle. The cooling half happens from 0 to 180 deg of crank angle when the flow goes from the cold side to the hot side, and the heating half happens from 180 to 360 deg. When zero TCR was present (base case), the mean Nusselt number curves for the two halves looked the same. However, with infinite TCR introduced, the heating half of the cycle shows a higher mean Nusselt number.

In terms of heat loss, Table 8 shows the results of integrating the enthalpy loss and the conduction loss over the whole cycle. In the case of the solid conduction, increasing the TCR from zero (base case) to infinite has resulted in a reduction of 54.7%. The enthalpy loss has increased by 13.8%. However, the total loss has decreased by only 14.0%. This suggests that it is a good idea to increase the TCR to reduce the heat loss; but the overall impact of a change from zero to infinite TCR is perhaps less than might be expected due to increased enthalpy flux loss. (This is approximated for the case of the 3-D involute-foil disks by alternating orientation of the involute-foil segments and offsetting separating ring locations, in adjacent disks, thus greatly reducing the contact area and increasing thermal resistance between disks.)

3. *Effect of Changing the Oscillation Amplitude*

The increase of the oscillation amplitude results in an increase of the maximum Reynolds numbers at 90 and 270 deg crank angle (CA). The friction factor has dropped, which is consistent with the steady-state simulations. When the Reynolds number is increased, the friction factor becomes smaller. The results show that the Nusselt number stays much the same.

In terms of heat loss, Table 9 shows the results of integrating the enthalpy loss and the conduction loss over the whole cycle, for the base case, and the increased oscillation-amplitude case.

A reduction in conduction loss occurred after the oscillation amplitude was increased by a factor of 3. However, due to the higher flow, the enthalpy loss increased by a factor of 10.6. The effect on the total heat loss is an increase by a factor of 6.6. The reduction in the axial solid conduction is attributed to the higher radial heat flow between gas and metal due to the higher instantaneous gas mass flow.

4. *Effect of Changing the Oscillation Frequency*

The effect of increasing the oscillation frequency was also studied. A frequency that is 3 times the base-case frequency was chosen for testing this effect. Therefore, frequency increased from 27.98 to 84 Hz while the Valensi number Re_ω or Va increased from 0.229 to 0.687; this also increased $Re_{\max}$ by a factor of 3. A change in frequency would alter both the fluid flow and the heat transfer behavior.

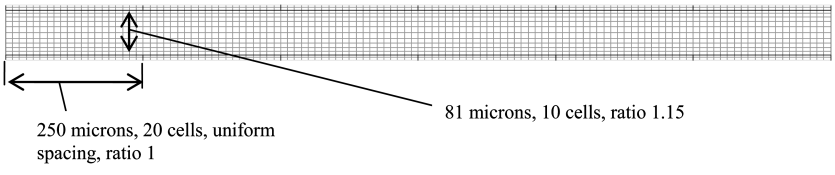

Fig. 14 Two-dimensional 20 × 10 grid.

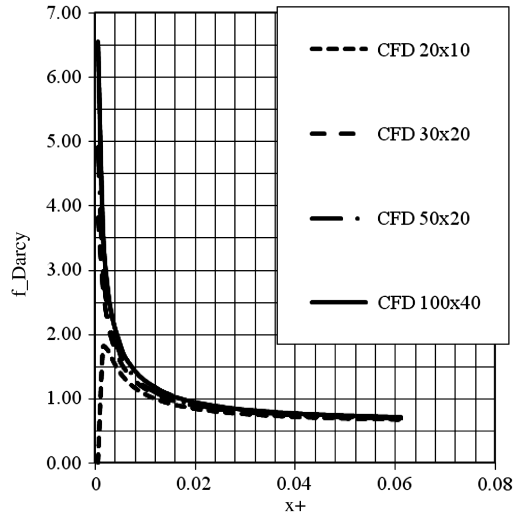

Fig. 15 Grid-independence study: Darcy friction factors f_{Darcy} as functions of dimensionless length x^+ at Reynolds number $Re = 150$ [for grids/segment of 20 × 10, 30 × 20, 50 × 20, and 100 × 40 (horizontal × vertical)].

In terms of heat loss, Table 10 shows the results of integrating the enthalpy loss and the conduction loss over the whole cycle for the base case ($Re_{\max} = 50$, $Re_\omega = 0.229$), the increased oscillation-amplitude case ($Re_{\max} = 150$, $Re_\omega = 0.229$), and the increased oscillation-frequency case ($Re_{\max} = 150$, $Re_\omega = 0.687$).

For the increased oscillation-frequency case, a 14% reduction in the axial conduction took place, whereas an increase (by a factor of 7.8) in the enthalpy flux occurred when compared with the base case. The net effect is about a factor of 5.0 increase in the total axial heat loss. Again, the reduction in axial solid conduction is attributed to the higher radial heat flow between gas and metal due to the higher instantaneous gas mass flow.

5. *Effect of Changing the Solid Material*

The impact of solid-material properties on performance are of interest. Pure metals are known to have higher conductivity than

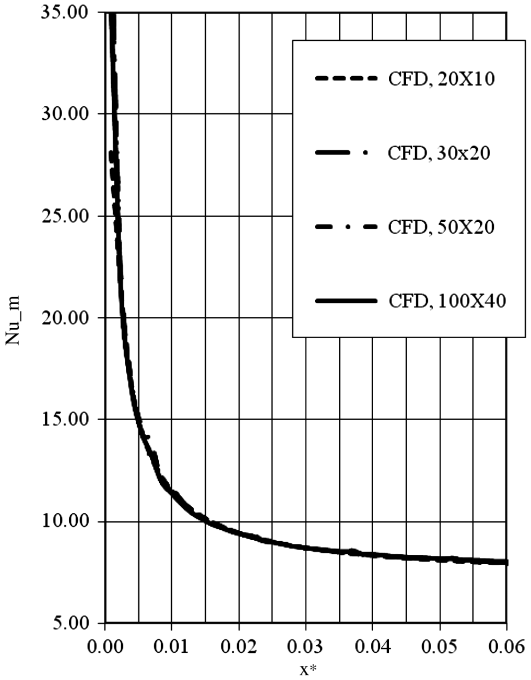

Fig. 16 Grid-independence study: Mean Nusselt numbers Nu_m as functions of dimensionless length x^* at Reynolds number $Re = 150$ [for grids/segment of 20 × 10, 30 × 20, 50 × 20, and 100 × 40 (horizontal × vertical)].

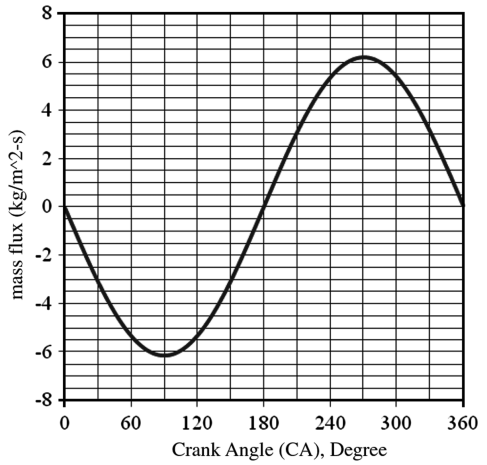

Fig. 17 Mass-flux forcing function as a function of crank angle in degrees for the base-oscillatory-flow case.

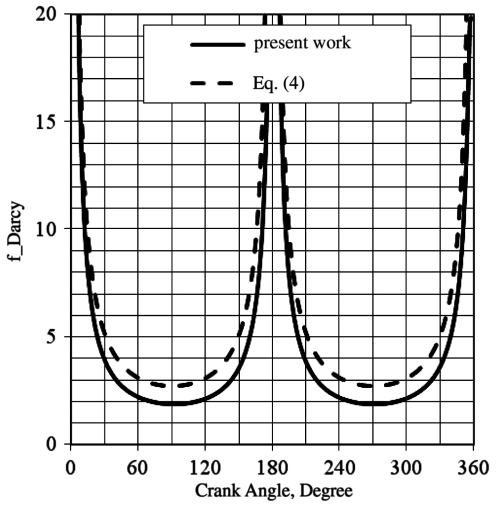

Fig. 18 Darcy friction factors f_{Darcy} as functions of crank angle in degrees. Comparisons of values calculated from 2-D CFD base-oscillatory-flow case (50 × 20 grids/segment) with Gedeon involute-foil correlation of Eq. (4).

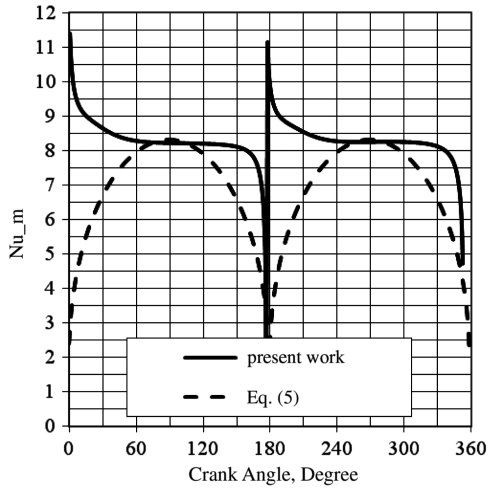

Fig. 19 Mean Nusselt numbers Nu_m as functions of crank angle in degrees. Comparison of values calculated from 2-D CFD base-oscillatory-flow case (50 × 20 grids/segment) with Gedeon involute-foil correlation of Eq. (5) (CFD assumes perfect thermal contact between layers, or zero thermal contact resistance).

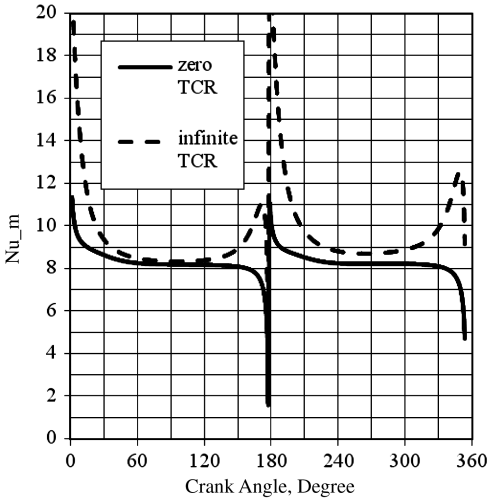

Fig. 20 Mean Nusselt numbers Nu_m as functions of crank angle in degrees. Comparison of values calculated from 2-D CFD oscillatory-flow cases (50 × 20 grids/segment) for 1) zero TCR (perfect thermal contact, base case) and 2) infinite TCR (adiabatic contact or perfect insulation).

alloys. Nickel was chosen for fabrication of the prototype test regenerator, due to limitations of cost and time (because a nickel regenerator could be fabricated via LiGA alone). However, nickel has a higher conductivity than SS (the preferred material) by about 5.5 times. For this comparison of nickel and SS materials, the contact between layers has been set to infinite TCR; thus, the reference SS case for this material study was not the base case (which had zero TCR). Infinite TCR is closer to the real 3-D geometry, due to the reduced contact area between the disks. As expected, no change in the friction factor was detected upon changing the material from SS to nickel. Figure 21 shows the behavior of the mean Nusselt number upon changing the material. Because of the higher conductivity of the nickel, the wall temperature profile was flatter than that for SS for the length of one layer, between two interfaces of infinite TCR. That should cause a change in the heat transfer. Note that Fig. 21 compares the cases of nickel with infinite TCR (adiabatic contact), SS with infinite TCR (adiabatic contact), and the case of SS with zero TCR (perfect contact, the base case).

The results show that, for infinite TCR between sections, the mean Nusselt number has increased overall for nickel compared to that for SS, especially at low Reynolds numbers (i.e., near flow reversals at ∼180 and 360 deg). Again, this is explained by the fact that, within a given layer, the nickel temperature profile is flatter, resulting in higher temperature differences between the wall and the fluid. The lower conductivity SS material can maintain a steeper temperature profile within one layer. This steeper profile is closer to the bulk-temperature profile of the fluid, leading to smaller temperature differences between fluid and solid. A comparison of the axial heat losses for nickel and SS is given in Table 11 (both with infinite TCR or adiabatic contact at the interfaces between layers).

In this case, a 36.3% increase in the axial conduction took place, whereas a decrease (by 5.1%) in the enthalpy flux occurred when nickel is compared with SS, both cases with infinite TCR between layers. The net effect is about a 3.8% increase in the regenerator axial heat loss using nickel. The increase in the axial conduction is attributed to the higher thermal conductivity of nickel (compared to SS). The infinite TCR approximates the effect of the limited surface-area contact between disks and greatly reduces the impact of nickel's 5.5 times greater (than SS) thermal conductivity.

B. Results of Model 2, Three-Dimensional Computational Fluid Dynamics Calculations for Straight-Channel-Layers

As discussed earlier, the grid for the involute-foil problem is quite dense and it was not feasible for use in oscillatory-flow simulations. The 3-D straight-channel grid was subjected to oscillatory-flow boundary conditions and the results follow (see geometry in Fig. 12).

1. Steady Flow Simulation (Model 2, Three-Dimensional, Straight-Channel Layers)

A 3-D steady-state simulation at a Reynolds number of 50 was performed to compare with the literature and with the 2-D results. This comparison is based on the Darcy friction factor plotted against the dimensionless hydrodynamic axial coordinate x^+. The same correlation from Shah [9], discussed earlier, is used. In Fig. 22, the Shah correlation is below the 2-D CFD results in the entry section and then matches well for larger values of x^+.

Also seen in Fig. 22, the 3-D results agree well with the 2-D results for the first layer. But upon entering the second layer, the flow

Table 8 Heat-loss comparison of zero-TCR base case to infinite-TCR case

	Enthalpy loss, W	Change	Conduction loss, W	Change	Total loss, W	Change
Base case	1.722	——	1.174	——	2.896	——
Infinite TCR	1.960	+13.8%	0.531	−54.7%	2.491	−14.0%

Table 9 Heat-loss comparison of base case ($Re_{max} = 50$) and increased oscillation-amplitude case ($Re_{max} = 150$)

	Enthalpy loss, W	Change	Conduction loss, W	Change	Total loss, W	Change
Base case	1.722	——	1.174	——	2.896	——
$Re_{max} = 150$	18.249	10.6 times	0.956	−18.6%	19.204	6.6 times

Table 10 Heat-loss comparison of base case ($Re_{max} = 50$, $Re_\omega = 0.229$), the increased oscillation-amplitude case ($Re_{max} = 150$, $Re_\omega = 0.229$), and the increased oscillation-frequency case ($Re_{max} = 150$, $Re_\omega = 0.687$)

	Enthalpy loss, W	Change	Conduction loss, W	Change	Total loss, W	Change
Base case $Re_{max} = 150$, $Re_\omega = 0.229$	1.722	——	1.174	——	2.896	——
Inc. osc. amplitude $Re_{max} = 150$, $Re_\omega = 0.229$	18.249	10.6 times	0.956	−18.6%	19.204	6.6 times
Inc. osc. frequency $Re_{max} = 150$, $Re_\omega = 0.687$	13.466	7.8 times	1.009	−14.1%	14.474	5.0 times

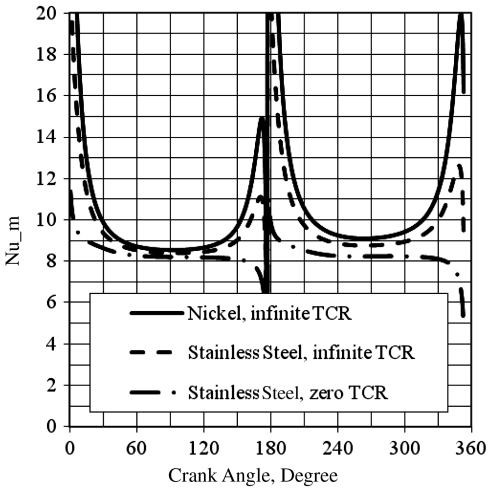

Fig. 21 Mean Nusselt number comparison between nickel and stainless steel, both with infinite TCR (adiabatic contact) between layers, and the base case (stainless steel, zero TCR or perfect contact).

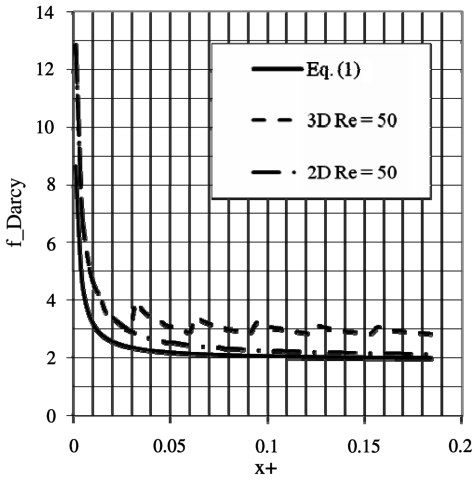

Fig. 22 Three-dimensional straight-channel layers, steady flow, friction-factor comparisons with 2-D results and Shah [9] literature correlation, all at Reynolds number $Re = 50$.

encounters some resistance from the perpendicularly oriented second layer. That is where the friction factor goes up and departs from the agreement with the 2-D results. Then, the flow tries to settle again until it encounters another geometry change upon entry into the third layer. As it moves through the stack of layers, the behavior of the fluid flow settles into periodicity, with small increases in friction factor upon entering each layer and with an average value above the 2-D prediction. This behavior was expected and the simulation provided an answer regarding the magnitude of the friction-factor increase.

To characterize the heat transfer, the mean Nusselt number is plotted with respect to the dimensionless thermal axial coordinate x^* in Fig. 23 and is compared to the results from the 2-D simulations and the correlation developed by Stephan [10]. As discussed earlier, the alternating orientation of the layers is expected to improve the heat transfer, relative to 2-D and uniform-channel flow. That should result in higher 3-D Nusselt number values at each flow-channel discontinuity; this can be observed in Fig. 23.

2. Oscillatory-Flow Simulation, Base Case (Three-Dimensional, Straight-Channel Layers)

For the 3-D straight-channel oscillatory-flow simulations, the same forcing function for the mass flux as in the 2-D simulations was used [see Eq. (6)]. As in the 2-D simulations, it took about 10 cycles to establish cycle-to-cycle convergence. The expectation again was that both the friction factor and the Nusselt number from the 3-D results would be higher.

As for the 2-D simulations, the friction factor is plotted (see Fig. 24) against the crank angle in degrees and compared to the 2-D case and the experimental correlation for involute foil [Eq. (4)].

As expected, the 3-D friction-factor values are higher than the 2-D results at all crank angles and are more in line with the experimental involute-foil correlation values from [Eq. (4)]. The mean Nusselt number results determined from the 3-D simulation are compared (see Fig. 25) with the 2-D results and the experimental involute-foil correlation from [Eq. (5)]. As mentioned earlier, the correlation averages the Nusselt number over the length of a stack of layers, whereas the present work uses only the length of one layer to obtain the mean Nusselt number. As expected, the Nusselt number values are higher than the values for the 2-D parallel-plate simulation and also are higher than the maximum value generated by Eq. (5).

3. Effect of Changing the Thermal Contact Resistance (Three-Dimensional, Straight-Channel-Layers)

As in the 2-D work, to study the effect of TCR between the layers, an infinite-TCR condition was imposed at the interfaces between the layers (replacing the zero TCR of the base case). The expectation is that the friction factor will not change when compared with the perfect contact case. However, the mean Nusselt number should behave similar to how it behaved when the same condition was imposed in the 2-D study. That is, the Nusselt number should increase overall, especially at the low Reynolds numbers that are encountered when the flow switches direction (near 180 and 360 deg). Figure 26 shows a comparison of the mean Nusselt number behavior among the 3-D zero-TCR (perfect contact) and the infinite-TCR (adiabatic contact) cases and the infinite-TCR (adiabatic contact) 2-D case. When compared to the 3-D zero-TCR case (i.e., perfect contact), the infinite-TCR (adiabatic contact) case has higher mean Nusselt number, especially in the regions of lower Reynolds numbers close to where the flow reverses. This was expected and it is similar to what happened in 2-D when the infinite-TCR condition was imposed.

C. Results of Model 1, Three-Dimensional Steady Flow Simulation of Involute-Foil Layers

In this section, the results for the 3-D involute-foil-layer simulations (see Fig. 11) are presented and discussed. This 3-D computational domain resembles more closely the actual microfabricated design in terms of the shape of the channel. However, the attempt to capture the geometry of the channel better resulted in a dense grid. Even after reducing the length of the stack to only two layers, the cell count was close to 2.7 million. As explained earlier, one can use a two-layer-long unit repeatedly by taking the velocity and temperature profile from the outlet and applying it back to the inlet to simulate a longer stack. The drawback of this technique is that oscillatory-flow simulation is not possible. Instead of one oscillatory-flow run, simulations have been performed using steady-state conditions at several Reynolds numbers.

The 3-D involute-foil grid actually consists of two types of grids, half- and full-length, with a repeating unit consisting of a one half-layer entry, a full layer, and a one half-layer exit (see Fig. 11). Cutting the first layer in half allows for the two grids to line up properly when

Table 11 Heat-loss comparison between stainless steel and nickel materials, both with infinite TCR (or adiabatic contact) at interfaces between layers (or disks)

	Enthalpy loss, W	Change	Conduction loss, W	Change	Total loss, W	Change
Infinite TCR and SS	1.960	——	0.531	——	2.491	——
Infinite TCR and nickel	1.862	−5.1%	0.724	+36.3%	2.586	+3.8%

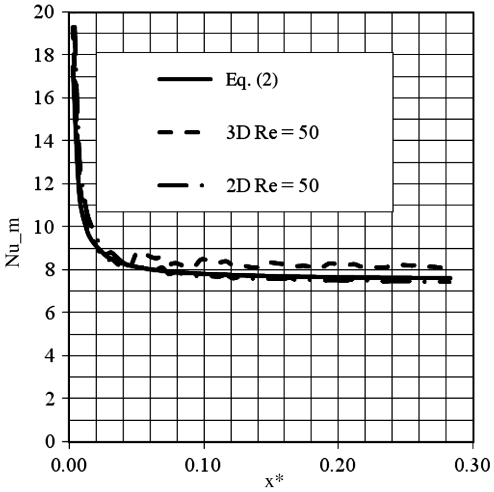

Fig. 23 Three-dimensional straight-channel layers, steady flow, mean Nusselt number comparisons with 2-D results and Stephan [10] literature correlation, all at Reynolds number $Re = 50$.

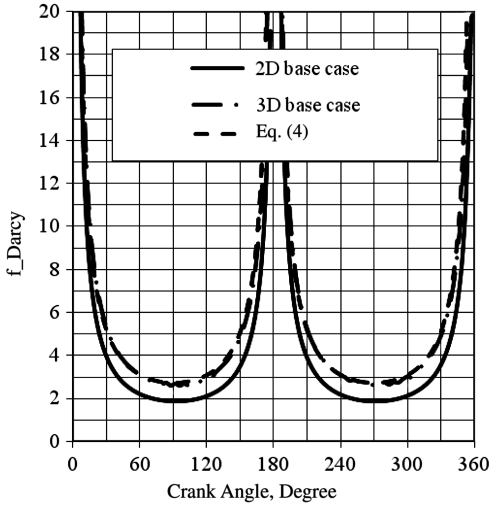

Fig. 24 Three-dimensional straight-channel layers, oscillatory-flow, friction-factor comparison to 2-D base-case oscillatory-flow results and the Gedeon [Eq. (4)] experimental involute-foil correlation.

passing the boundary conditions (profile) from one grid to the other. By the same token, two repeating units will line up properly so that the boundary profile can be passed, where the geometry is continuous. As shown in Fig. 11, the repeating-grid unit captures one full

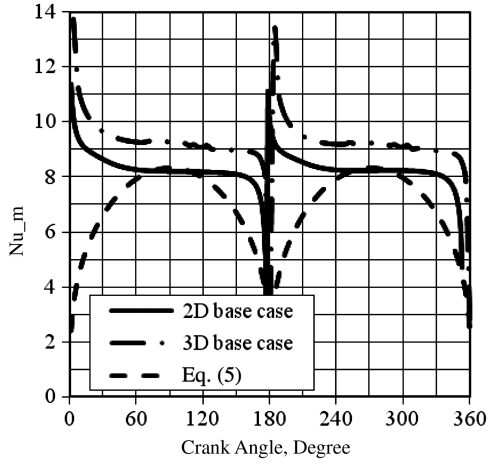

Fig. 25 Three-dimensional straight-channel layers, oscillatory-flow, mean Nusselt number comparison to 2-D base-case oscillatory-flow results and the Gedeon [Eq. (5)] experimental involute-foil correlation.

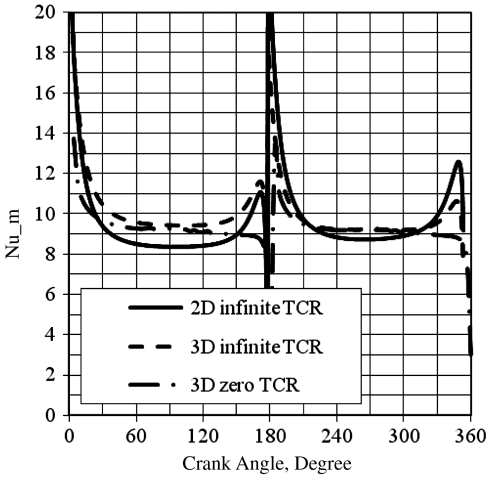

Fig. 26 Mean Nusselt number comparison for 3-D straight-channel layers, oscillatory-flow cases, with zero TCR (perfect contact) and infinite TCR (adiabatic contact) between layers, and for the 2-D oscillatory-flow infinite-TCR (adiabatic contact) case.

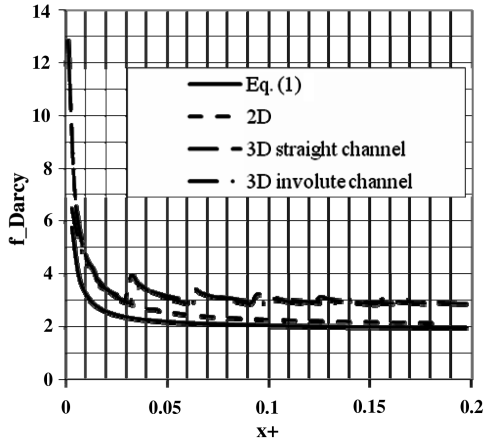

Fig. 27 Steady-state friction-factor comparison at Reynolds number $Re = 50$ as a function of dimensionless length. Calculated via the 3-D involute-foil and straight-channel layer simulations, the 2-D parallel-plate simulation, and compared with the Shah [9] correlation.

involute-foil channel in the middle. The other channels are also simulated as full because of the periodic boundary conditions applied to the sides. In fact, when periodicity is considered, this grid simulates a full ring of channels. The contact between the layers is perfect, that is, the TCR is zero.

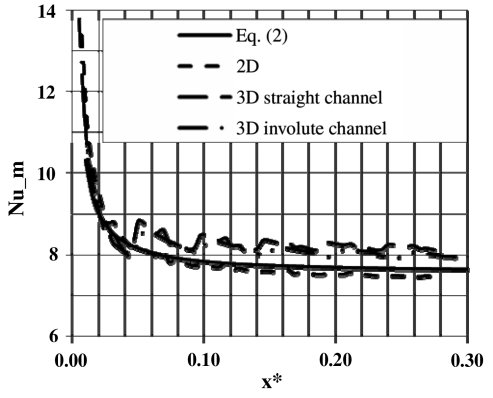

Fig. 28 Steady-state mean Nusselt number comparisons at Reynolds number $Re = 50$ as a function of dimensionless length. Calculated via the 3-D involute-foil and straight-channel layer simulations, the 2-D parallel-plate simulation, and compared with the Stephan [10] correlation.

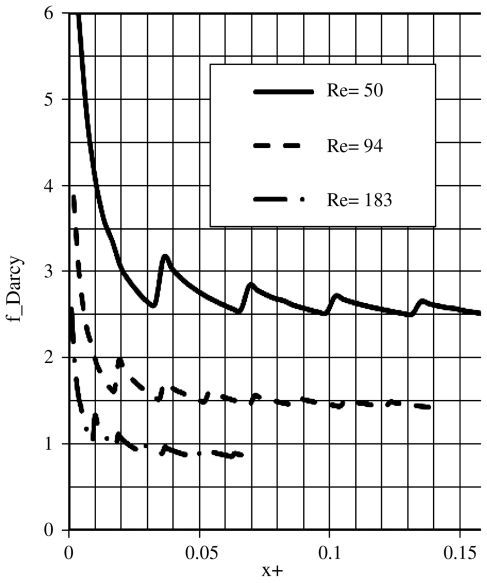

Fig. 29 Steady 3-D involute-foil simulation friction factor at different Reynolds numbers $Re = 50$, 94, and 183, as a function of the dimensionless length x^+.

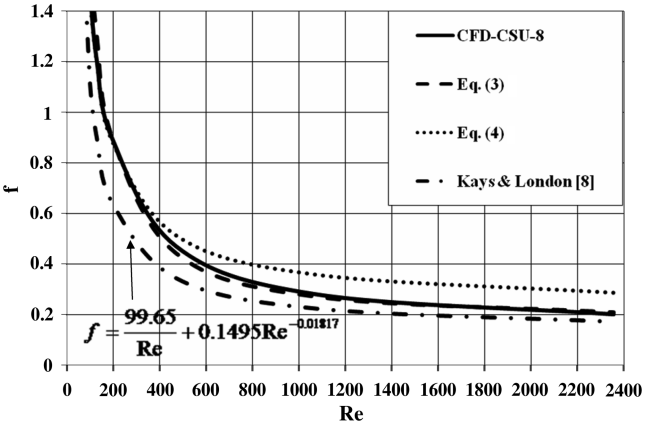

Fig. 30 Three-dimensional involute-foil simulation friction factor (CFD-CSU-8) compared with UMN large-scale measurements (8 and 10 layers), Gedeon involute-foil experimental correlation (GA-42-1, original stacking), and Kays and London [8] staggered-plate correlation.

Meshing this geometry presented a considerable challenge. Even though the channels were insured to line up properly, to not get discontinuities when passing the boundary profile, one has to ensure that the cell coordinates of the exit face match the cell coordinates of the inlet face. The ends of the channel with their round shape did not allow for a structured mesh and an unstructured mesh had to be employed. However, the generation of the unstructured mesh is harder to control when it comes to matching cell coordinates between inlet and outlet faces. This required linking the inlet and the outlet faces, which is a tedious process.

1. Steady-State, $Re = 50$, Comparisons of Friction Factor and Mean Nusselt Number

As for the 2-D parallel plate and the 3-D straight-channel layers, a 3-D involute-foil-layers simulation at $Re = 50$ was performed. To compare with the 2-D results and with the literature, the Darcy friction factor is plotted (see Fig. 27) against the dimensionless hydrodynamic axial coordinate x^+. The same literature correlation, Shah [9], is used.

The 3-D involute-foil-layers simulation shows a variation in friction factor (the saw shape) similar to the 3-D straight-channel layers, as expected. One thing to keep in mind is that the length of the involute-foil layer is 15 μm longer in the flow direction than the 3-D straight-channel layer. While work was in progress on this project, it was learned that the actual fabricated layers were shorter than originally intended. The 3-D straight channel was adapted to the shorter length and simulations were performed that way. However, the 3-D involute-foil layer length simulated was kept at the original length. The preceding comparison captures this difference graphically by showing that the layer-to-layer rise in friction factor for the 3-D involute-foil layers happens after the rise shown by the 3-D straight-channel layers.

To characterize the heat transfer, the 3-D involute-foil mean Nusselt number is plotted (see Fig. 28) with respect to the thermal axial coordinate and is compared to the results from the 2-D simulation, 3-D straight-channel simulation, and the correlation developed by Stephan [10]. The variation in mean Nusselt number Nu_m is similar to that encountered for the 3-D straight-channel grid. The out-of-step layer-to-layer transition is again explained by the previously described difference in the lengths of the layers.

2. Summary: Steady Three-Dimensional Involute-Foil Friction-Factor Results for All Reynolds Numbers

Simulations at other values of Reynolds number were performed to determine the variation of the friction factor with the Reynolds number. A total of six Reynolds numbers were used: $Re = 50$, 94, 183, 449, 1005, and 2213.

Figure 29 compares the variation of the friction factor at Reynolds numbers of 50, 94, and 183. The friction factor is lower at higher Reynolds numbers, as expected. As in previous simulations, the regular friction-factor increases observed at the transition from layer to layer are present at the other Reynolds numbers. The fact that the transitions do not line up is an artifact of the plotting versus the dimensionless axial coordinate x^+, which includes the Reynolds number in the denominator.

In Fig. 30, the results obtained from the 3-D involute-foil simulations have been compared with experiments done by the UMN on 8- and 10-layer large-scale stacks. The same graph shows results from a correlation developed by Kays and London [8] for staggered-plate heat exchangers and Eq. (4) based on involute-foil experiments performed in the NASA/Sunpower oscillating-flow test rig. The

Table 12 Summary for all cases examined for model 3

Number	Description	Enthalpy loss, W (change from baseline, except case 5)	Conduction loss, W (change from baseline except case 5)	Total, W (change from baseline except case 5)
1	Baseline case: $Re_{max} = 50$, $Re_\omega = 0.229$, TCR = 0, SS	1.722	1.174	2.896
2	$Re_{max} = 50$, $Re_\omega = 0.229$, TCR = inf ., SS	1.96 (+13.8%)	0.531 (−54.7%)	2.491 (−14%)
3	$Re_{max} = 150$, $Re_\omega = 0.229$, TCR = 0.0, SS	18.249 (10.6 times)	0.956 (−18.6%)	19.204 (6.6 times)
4	$Re_{max} = 150$, $Re_\omega = 0.687$, TCR = 0.0, SS	13.466 (7.8 times)	1.009 (−14.1%)	14.474 (5 times)
5	$Re_{max} = 50$, $Re_\omega = 0.229$, TCR = inf ., nickel (compared with case 2)	1.862 (−5.1%)	0.724 (+36.3%)	2.586 (+3.8%)

results from the current 3-D involute-foil simulations match very well with the UMN experiments. Both the CFD and UMN data match very well with Gedeon's correlation, Eq. (4), at the low end of the Reynolds number range (∼100–200). However, Eq. (4) provides higher friction-factor values at the high end of the Reynolds number range (∼1000). This may be due to the roughness associated with the EDM cutting process.

VII. Conclusions

Three different computational models were identified as good candidates for modeling the problem at hand. One was a 2-D domain (model 3) and the other two were 3-D domains (models 1 and 2). Because model 3 was the least expensive computationally (and closely simulates our problem) it was studied more extensively. The following conclusions are provided for each model starting with model 3, then model 2, and finally model 1.

The 2-D parallel-plate steady-state simulations showed good agreement with the correlations from the literature [9,10]. A baseline case was chosen for this study using helium as the working fluid at pressure = 2.5E06 Pa (25 atm), and SS solid material with zero TCR between the six layers. The oscillation frequency and amplitude chosen resulted in maximum Reynolds number $Re_{\max} = 50$ and Valensi number $Re_{\omega} = 0.229$. For this base case, the enthalpy loss computed throughout the cycle was equal to 1.722 W, whereas the axial conduction loss was equal to 1.174 W with a total axial heat-transfer loss of 2.896 W. This total value, plus viscous-flow losses, must be minimized for optimum regenerator design. Table 12 shows this case as well as four other cases examined for model 3.

Changing the solid TCR from zero to infinity between the layers (case 2) resulted (compared to case 1) in a 54.7% reduction in the axial conduction, a 13.8% increase in the enthalpy loss, with a 14% reduction in the regenerator axial heat loss. Increasing the velocity amplitude of the oscillation (by a factor of 3), case 3, resulted (compared to case 1) in an 18.6% reduction in the axial conduction, an increase (by a factor of 10.6) in the enthalpy loss, with a 6.6 increase in the regenerator axial heat loss. Increasing the frequency of the oscillation (by a factor of 3), case 4, resulted (compared to case 1) in a 14% reduction in the axial conduction, an increase by a factor of 6.9 in the enthalpy loss, with a net effect of about a factor of 5.8 increase in the regenerator heat loss. Increasing the thermal conductivity of the solid material (by changing the solid material from stainless steel to nickel), case 5, resulted (compared to case 2, with both cases having infinite TCR) in a 36.3% increase in the axial conduction, a 5% decrease in the enthalpy loss, with a net effect of about 3.8% increase in the regenerator heat loss.

It can be seen from the preceding cases (cases 1 and 2) that changing the TCR from zero (lower bound) to infinity (upper bound) has the net effect of decreasing the regenerator heat loss. In the case of SS (case 2), the axial conduction reduction (−54.7%) offsets the increase in the enthalpy loss (13.8%) by a net decrease in the heat loss (−14%). However, this is not the case for nickel (case 5) where the thermal conductivity (5.5 times greater than SS) resulted in a net increase in heat loss of 3.8% (see cases 2 and 5). Both changing the velocity amplitude of the oscillation or the frequency resulted in an increase by a big factor (about 9 times) in the enthalpy loss.

For the 3-D straight-channel layer steady-state simulation, both the friction factor and the mean Nusselt numbers are in perfect agreement with the 2-D simulation values in the first layer. Upon entering the second layer, the 3-D effects become obvious and they persist as the axial coordinate advances. At the entrance of every layer, the forced reorientation of the flow results in small rises of both the friction factor and the mean Nusselt number with subsequent decreases as the flow settles into each new layer. Overall, the plots of the 3-D friction factor and the mean Nusselt number tend to flatten out as the flow reaches a fully developed condition, but at values above the 2-D simulation results.

For the oscillatory-flow simulations of the 3-D straight-channel layers, the friction factor shows an overall increase compared to the 2-D oscillatory-flow simulation and is in excellent agreement with the experimental involute-foil correlation [Eq. (4)]. The mean Nusselt number also shows an overall increase compared to the results from the 2-D simulation. It also shows a higher value when compared to Eq. (5) at the maximum Reynolds number. The shapes of both the friction factor and mean Nusselt number curves are similar to the shapes observed in the 2-D simulations. So the effect of going from 2-D to 3-D resulted in shifts upward of both friction factor and mean Nusselt number curves, as might be expected because the 2-D simulations do not include the flow perturbations resulting from flow around the ends of the foil layers.

Changing the TCR from zero to infinite between the solid layers in the 3-D straight-channel layers with oscillating flow had no effect on the friction factor, as expected. However the mean Nusselt number increased overall but with a more pronounced increase at the crank angles near where the flow switches direction. Although the actual values for the mean Nusselt number are higher in the 3-D simulations, the more expedient 2-D simulations capture well the behavior of the mean Nusselt number as the TCR is changed. It should be noted that, although the experimental correlation for Nu was obtained for 42 layers, the calculation made in model 2 was only done for one layer.

As with the 3-D straight-channel layers, the simulations for the 3-D involute-foil layers show increases in both friction factor and mean Nusselt number at the geometric transitions between the layers. Furthermore, at $Re = 50$, these increases are similar for the 3-D straight channel and the 3-D involute-foil simulations. From this similarity, one can infer that using a simpler grid such as that used for the 3-D straight-channel layers can capture to a good extent the steady-state three-dimensional effects of the 3-D involute-foil layers for low Reynolds numbers. This is important in terms of the practicality of doing CFD simulations. Although more computing power is available now more than ever, the researcher still must compromise between computing time and accuracy.

The overall friction factor matched well the experimental results (obtained from Ibrahim et al. [4]). That lends credence to the simulations performed for the 3-D involute-foil layers. The detailed work that went into constructing the grid, running the CFD simulations, and postprocessing the data provided meaningful results, validated by experiment. By their nature, the simulations can, in a more expedient way, go beyond what the experiments can do and provide further predictions for optimization or comparison with other designs.

The technique of analyzing a repeating unit recursively has also been validated. That allows for steady-state simulations of a stack consisting of a large number of layers by using a repeating unit that is only two layers thick. That, in turn, not only saves on computation time and resources but also makes the simulation of a large stack feasible.

Acknowledgments

We are grateful for sponsorship of this effort by the NASA Headquarters Science Mission Directorate and the Radioisotope Power System Program and for the support of the NASA Glenn Research Center at Lewis Field under NASA Contract NAS3-03124, for which the Contracting Officer's Technical Representative was Roy Tew. We wish to acknowledge the valuable guidance we received from our team of advisors: James Cairelli (retired) and Randy Bowman, both of NASA Glenn Research Center at Lewis Field, and David Berchowitz at Global Cooling, Inc.

References

[1] Organ, A. J., "Two Centuries of Thermal Regenerator," *Proceedings of the Institution of Mechanical Engineers, Part C, Journal of Mechanical Engineering Science*, Vol. 214, No. C1, 2000, pp. 269–288. doi:10.1243/0954406001522958

[2] Ibrahim, M. B., Veluri, S., Simon, T., and Gedeon, D., "CFD Modeling of Surface Roughness in Laminar Flow," AIAA Paper 2004-5585, Aug. 2004.

[3] Ruhlich, I., and Quack, H., "Investigations on Regenerative Heat Exchangers," *Cryocoolers 10*, edited by R. G. Ross Jr., Klewer Academic, Norwell, MA, 1999, pp. 265–274.

[4] Ibrahim, M. B., Danila, D., Simon, T., Mantell, S., Sun, L., Gedeon, D., Qiu, S., Wood, J. G., Kelly, K., and McLean, J., "A Microfabricated Segmented-Involute-Foil Regenerator for Enhancing Reliability and Performance of Stirling Engines: Phase II Final Report for the Radioisotope Power Conversion Technology NRA Contract NAS3-03124," NASA Contract Rept. 2007-215006, 2007.

[5] Ibrahim, M. B., Keister, J., Sun, L., Simon, T., Mantell, S. C., Gedeon, D., Guidry, D., Qiu, S., and Wood, G., "Assessing the Performance of a Microfabricated Regenerator for Stirling Space-Power Convertor," AIAA Paper No. 2005-5597, Aug. 2005.

[6] Ibrahim, M. B., Tew, R., Gedeon, D., Wood, G., and McLean, J., "Microfabrication of a Segmented-Involute-Foil Regenerator, Testing in a Sunpower Stirling Convertor, and Supporting Modeling and Analysis," AIAA Paper No. 2008-5716, July 2008.

[7] Fluent 6.3 User Guide, Fluent, Inc., Santa Clara, CA, 2005, www.fluent.com.

[8] Kays, W., and London, A., *Compact Heat Exchangers*, 2nd ed., McGraw–Hill, New York, 1964, p. 213.

[9] Shah, R. K., "A Correlation for Laminar Hydrodynamic Entry Length Solutions for Circular and Noncircular Ducts," *Journal of Fluids Engineering*, Vol. 100, 1978, pp. 177–179.

[10] Stephan, K., "Warmeubergang und druckabfall bei nicht ausgebildeter Laminarstromung in Rohren und in ebenen Spalten," *Chemie-Ingenieur-Technik*, Vol. 31, No. 12, 1959, pp. 773–778. doi:10.1002/cite.330311204

[11] Shah, R. K., and London, A. L., *Laminar Flow Forced Convection in Ducts*, Academic Press, New York, 1978.

[12] Danila, D., "CFD Investigation of Fluid Flow and Heat Transfer in an Involute Geometry for Stirling Engine Applications," M.S. Thesis, Cleveland State Univ., Cleveland, OH, 2006.